Clim Dyn
DOI 10.1007/s00382-011-1085-2

Sensitivity of the Humboldt Current system to global warming: a downscaling experiment of the IPSL-CM4 model

Vincent Echevin · Katerina Goubanova · Ali Belmadani · Boris Dewitte

Received: 16 August 2010 / Accepted: 21 April 2011

Abstract The impact of climate warming on the seasonal variability of the Humboldt Current system ocean dynamics is investigated. The IPSL-CM4 large scale ocean circulation resulting from two contrasted climate scenarios, the so-called Preindustrial and quadrupling CO_2, are downscaled using an eddy-resolving regional ocean circulation model. The intense surface heating by the atmosphere in the quadrupling CO_2 scenario leads to a strong increase of the surface density stratification, a thinner coastal jet, an enhanced Peru–Chile undercurrent, and an intensification of nearshore turbulence. Upwelling rates respond quasi-linearly to the change in wind stress associated with anthropogenic forcing, and show a moderate decrease in summer off Peru and a strong increase off Chile. Results from sensitivity experiments show that a 50% wind stress increase does not compensate for the surface warming resulting from heat flux forcing and that the associated mesoscale turbulence increase is a robust feature.

Keywords Regional climate change · Peru–Chile upwelling system · Mesoscale dynamics · Coastal upwelling

V. Echevin (✉) · A. Belmadani
LOCEAN, Paris, France
e-mail: vincent.echevin@locean-ipsl.upmc.fr

K. Goubanova · A. Belmadani · B. Dewitte
LEGOS, Toulouse, France

K. Goubanova · B. Dewitte
IMARPE, IGP, LEGOS, Lima, Peru

A. Belmadani
IPRC, International Pacific Research Center,
SOEST, University of Hawaii at Manoa, Honolulu, Hawaii

1 Introduction

The Humboldt Current system (HCS) is the most productive Eastern Boundary Upwelling System (hereafter EBUS) of the world ocean in terms of fisheries (Chavez et al. 2008). Driven by quasi-permanent upwelling-favorable winds which generate an intense upwelling of cold, nutrient-rich deep waters, it holds a thriving ecosystem, from plankton to abundant small pelagic fish stocks, which is very sensitive to climate variability at various time scales. Chavez et al. (2003) showed that the main ecosystem components (sardines, anchovies and marine birds) off Peru display significant variations at a wide range of temporal scales, from interannual ENSO-related variability to interdecadal variability in relation to the Pacific Decadal Oscillation occurring in the North Pacific. Given that climate change is occurring in many regions of the world as well as in the Eastern South Pacific (Falvey and Garreaud 2009), the consequences of these changes on the HCS oceanic conditions remain largely unknown. In particular, the impact of wind forcing and large scale ocean circulation changes on coastal upwelling remains a central issue. Along with this main concern, one may also question how the nearshore mesoscale circulation and associated offshore transport of water mass properties are modified in a warmer climate, and the potential consequences on the marine ecosystem. These are the background questions that motivate the present study.

In recent years, the World Climate Research Programme's (WRCP's) Working Group on Coupled Modelling (WGCM, http://www-pcmdi.llnl.gov/ipcc/about_ipcc.php) has made available to the scientific community an ensemble of coupled model simulations through the Coupled Model Intercomparison Project phase 3 (CMIP3), which aims at representing the evolution of large scale

Published online: 10 May 2011

oceanic and atmospheric conditions in the next decades under various emission scenarios of atmospheric CO_2. These simulations provide an invaluable tool to study global and regional climate change. However, global models generally have a rather coarse spatial resolution (~2–3° in the atmosphere, ~1–2° in the ocean), which does not allow an adequate representation of regional dynamical processes, such as the influence of the Andes mountains on the atmospheric circulation, or the role of the continental shelf and slope on coastal ocean dynamics. Thus, so-called downscaling methods need to be developed and used to represent the key features and processes at the appropriate spatial scales in these regions.

Oceanic downscaling relies particularly on the availability of momentum and heat flux forcing at the sufficient spatial and temporal resolution. This is all the more critical for EBUSs which are sensitive to the nearshore mesoscale (~O (10 km)) structures of the winds due to predominance of Ekman dynamics. Atmospheric downscaling is thus a necessary step in order to properly address such issue.

Several downscaling experiments have been performed in various EBUSs.

In the California upwelling system, Snyder et al. (2003) used a regional atmospheric circulation model to study the changes in surface wind stress and curl in the so-called "preindustrial" (hereafter PI) scenario, a reference scenario with CO_2 concentrations fixed to their preindustrial level (280 ppm), and the "doubling" (hereafter $2CO_2$) scenario, with CO_2 concentrations evolving at a rate of 1% per year from preindustrial level to doubling (560 ppm) before stabilizing (Meehl et al. 2007a). Their results showed an increase in upwelling-favorable winds during the upwelling season, with moderate changes in seasonality.

Off central Chile, Garreaud and Falvey (2009) used the PRECIS regional model (Jones et al. 2004) to downscale the HadCM3 outputs (Gordon et al. 2000; Pope et al. 2000) for the "present climate conditions" (20C3M), SRES A2 and B2 scenarios (Nakicenovic and Coauthors 2000). They evidenced a significant increase in alongshore winds off central Chile during the summer upwelling season.

Recently, Goubanova et al. (2010) used a statistical downscaling method to represent high resolution (~50 km) surface winds in the HCS from the outputs of the IPSL-CM4 model (Hourdin et al. 2006; Marti and Coauthors 2010). Two idealized climate scenarios were downscaled: PI and the "quadrupling" (hereafter $4CO_2$) scenario, with CO_2 concentrations evolving at a rate of 1% per year from preindustrial level to quadrupling (1,120 ppm) before stabilizing. They showed that on seasonal time scales, the alongshore wind increases by ~10–20% off Chile in $4CO_2$ with respect to PI, in agreement with results from Garreaud and Falvey (2009). Off Peru, alongshore wind decreases by ~10% in summer with hardly any change in winter. Nearshore wind stress curl also displays changes in its seasonal variations, a 10–20% curl increase (resp. decrease) in winter (resp. Summer) in the $4CO_2$ scenario with respect to PI off Peru, and an increase of up to 50% south of 25°S off Chile (Figure not shown).

Although most IPCC models predict an intensification of South Eastern Pacific anticyclone in a warmer climate which translates into an intensification of the coastal jet off Central Chile (Garreaud and Falvey 2009), the projections for the coastal range off Peru are more subtle due to the weaker amplitude and variability in surface atmospheric circulation over this region (Fig. 1). In particular, according to Bakun's hypothesis (Bakun 1990; Bakun and Weeks 2008; Bakun et al. 2010), alongshore winds off Peru (as well as in the other EBUSs) would increase under warmer conditions due to an enhanced thermal contrast between land and sea, which would in turn favour upwelling conditions. On the other hand, a decrease in the strength of the South Eastern Pacific branch of the trade winds may be expected due to a weakening of the basin-scale Walker circulation that is projected from coupled general circulation models (CGCMs) under increased atmospheric CO_2 concentration conditions (Vecchi and Soden 2007). The lack of long-term and densely sampled data sets, however, does not allow a confident diagnosis of the wind-stress trend along the coast of Peru/Chile from observations and its relationship with warmer conditions. This limits to some extent our understanding of the processes at work in controlling the upwelling conditions off the west coast of South America in a warmer climate.

Whereas several studies of the changes in atmospheric conditions in EBUSs already exist, very few studies of the EBUSs response of the ocean circulation to climate change have been performed, and none for the HCS. Auad et al. (2006) used a regional ocean model forced by downscaled surface winds, heat fluxes and ocean boundary conditions from a 36% CO_2 increase scenario in the California upwelling system. They evidenced an upwelling increase of cool deep waters forced by a wind stress increase, in agreement with Bakun's predictions (Bakun 1996). This wind-forced upwelling is strong enough to overcome the surface stratification increase caused by the greenhouse surface warming. This led to a moderate oceanic cooling at the surface, higher vertical velocities during the upwelling season and lower nearshore eddy activity, with respect to normal conditions.

Because of the peculiarities of each EBUS (Carr and Kearns 2003; Chavez and Messié 2009) and the complexity of ocean dynamics, the conclusions reached by Auad et al. (2006) cannot be extended to other upwelling systems. Taking into account complex dynamical processes—such as the local effects of coastline, bottom topography and

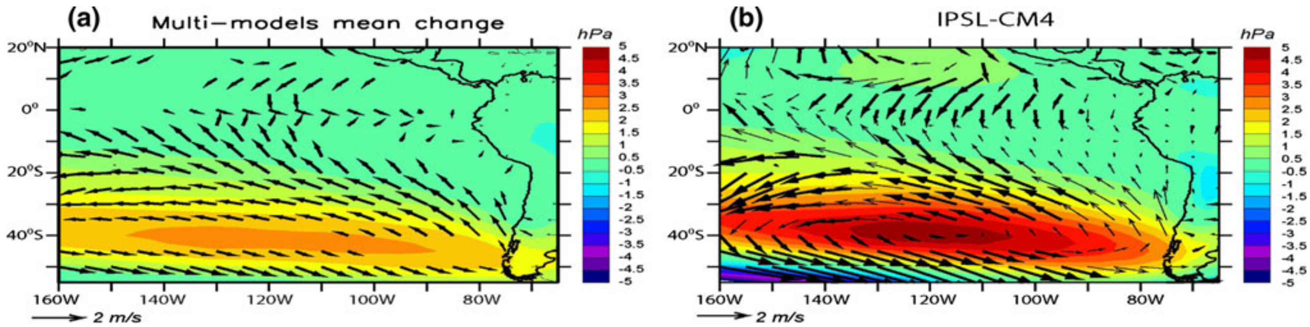

Fig. 1 **a** Difference in surface winds (*arrows*) and sea level pressure (*colour*) between experiments A2 (2081–2100) and 20C3M (1981–2000) calculated based on **a** a multi-model ensemble and **b** the IPSL-CM4 model. The wind difference for the multi-model ensemble is shown for the points where more than 75% of the CGCMs agree on the sign of the difference. The *bold arrows* at (**b**) indicate the regions where IPSL-CM4 surface wind change is significantly different (at the 90% confidence level) from the multi-model average change. The multi-model average was obtained by interpolating the outputs from 13 coupled GCMs runs performed for CMIP3 to a uniform 2.5° × 2.5° lat–lon grid, and subsequently averaging the long-term mean of each model. The CGCMs used are BCCR-BCM2.0, CGCM3.1(T47), CNRM-CM3,CSIRO-MK3.0, CSIRO-MK3.5, GFDL-CM2.0,GFDL-CM2.1,INGV-ECHAM4,INM-CM3.0, IPSL-CM4, MPIM-ECHAM5, MRI- CGCM2.3.2,GISS-ER (the data are available at http://www-pcmdi.llnl.gov/)

non-linear dynamics—on the regional circulation is required to study the response of the upwelling under warmer climate conditions. Simply put, a better understanding of the sensitivity of upwelling dynamics to anthropogenic forcing is needed in EBUSs, and particularly in the HCS.

In the present study, the impact of the climate change-related modification of large scale atmospheric and oceanic forcing on the regional circulation in the HCS is addressed. Our study is based on the comparison of the PI and $4CO_2$ climate IPSL-CM4 downscaled scenarios. Comparing these particular scenarios highlights the impact of climate change in an extreme and idealized framework, which allows to focus on the key processes at stake. It builds upon the work by Goubanova et al. (2010) which provides the momentum forcing at relatively high-resolution for the high-resolution oceanic model simulations performed in this study. In that sense the present study can be seen as a companion paper.

As the impact of climate change on interannual ENSO variability strongly influencing the HCS has been difficult to diagnose from ensemble models (van Oldenborgh et al. 2005; Guilyardi 2006; Meehl et al. 2007b; Guilyardi et al. 2009), we chose to focus on changes in the mean state and seasonal variability. Modifications of the cross-shore thermohaline and velocity structure, the upwelling intensity, and surface eddy kinetic energy, which diagnoses the intensity of the mesoscale circulation of particular interest for the transport of small pelagic fish larvae, are investigated in detail.

Two 30-year time periods accounting for the change in mean state and seasonal cycle under global warming were selected in the climate scenarios of IPSL-CM4 model of the IPCC data base, and downscaled using the ROMS (Regional Ocean Modelling System) model.

The paper is organized as follows: In Sect. 2, the selected climate scenarios and the downscaling methods are described. Modelling results from standard experiments and from sensitivity experiments in which wind stress is artificially modified are presented in Sect. 3. A summary and discussion are presented in Sect. 4, before some perspectives are outlined.

2 Methods

Among the climate models of the IPCC data base, the IPSL-CM4 model (Marti and Coauthors 2010) was selected. The motivation for choosing the IPSL-CM4 model was threefold: (1) the daily atmospheric outputs were available over an extended period of time, and for many variables which allowed to design a statistical atmospheric downscaling model (see Goubanova et al. (2010) for details); (2) this global model has been shown to reproduce realistically key aspects of the large scale circulation (cf. Sect. 3), which includes ENSO variability (Marti and Coauthors 2010; Belmadani et al. 2010) and the subtropical anticyclone (Garreaud and Falvey 2009); (3) the IPSL-CM4 response to global warming mimics the sensitivity of the IPCC multi-model ensemble mean. The response of sea level pressure and surface wind to global warming simulated by the IPSL-CM4 model is similar, in terms of spatial structure, to those estimated from a multi-model ensemble (Fig. 1, see also Goubanova et al. (2010)). Moreover, the response of key large scale oceanic parameters such as the local thermocline depth, the vertical stratification and the Equatorial Undercurrent (EUC) eastward flux into the Peru–Chile region (Table 1) in the IPSL simulations range with those from a selection of the most realistic CGCMs in the ESP (Belmadani et al. 2010). Selecting a single model among the entire IPCC model ensemble does offer a somewhat limited viewpoint on regional climate change. However, due to the computational cost of dynamical downscaling and since the paper focuses on the processes at work under global warming, this limitation is not detrimental for the purpose of the paper.

Two 30-year time periods were selected from the PI and $4CO_2$ scenarios, respectively: the 1970–1999 period from the PI scenario, and the 2120–2149 period from the $4CO_2$ scenario. Note that the calendar of the model years has no particular meaning since (1) they refer to idealized experiments without a realistic CO_2 forcing and (2) CGCMs are known to diverge from reality after a few years if not started with observed ocean–atmosphere initial conditions.

The IPSL-CM4 coupled model has a resolution of 3.75° (longitude) × 2.54° (latitude) in the atmosphere and 2° (longitude) × 1° (latitude) in the ocean. As briefly outlined in the introduction, a statistical downscaling method was applied in order to produce surface wind fields at a sufficiently high spatial resolution to adequately force the regional ocean model (see following paragraph). The IPSL-CM4 surface wind fields display unrealistic patterns near the coastline of the very coarse atmospheric model (see Goubanova et al. (2010)). In a nearshore band of O (∼100 km), which scales with the size of the atmospheric model grid, divergence of the Ekman transport at the coast and wind stress curl are the main forcing of upwelling, thus wind stress spatio-temporal variability needs to be adequately represented near the coast. For this purpose, a statistical method, which takes advantage of the relatively high-resolution QuikSCAT satellite wind products over the 2000–2008 period, was used to derive regional daily wind stress fields with 0.5° × 0.5° spatial resolution from the IPSL-CM4 large-scale outputs. Details on the method and its validation are described in Goubanova et al. (2010).

A dynamical downscaling method is used to represent the regional ocean circulation. The eddy-resolving ROMS regional ocean circulation model (Shchepetkin and McWilliams 2005) is used at a resolution of 1/6° in longitude times 1/6°cos(ϕ) in latitude (∼18 km) in a spatial domain covering 100°W–70°W, 15°N–40°S. This model configuration has open boundaries on its northern, western and southern sides. ROMS solves the hydrostatic primitive equations with a free surface explicit-scheme, and sigma coordinates on 31 vertical levels. Bottom topography from ETOPO2 (Smith and Sandwell 1997) has been interpolated on the model grid, smoothed to reduce pressure gradient errors and modified at the open boundaries to match bottom topography from the ORCA2 model (Madec et al. 1998) the ocean component of the IPSL-CM4 model. This model configuration is quite similar to that used in Colas et al. (2008), with a lower spatial resolution in our case.

ROMS is forced at the ocean–atmosphere interface by the downscaled wind stress. Heat and fresh water fluxes are taken directly from the IPSL-CM4 outputs. The heat flux includes a restoring term to a prescribed surface temperature field. As these fields have a coarse resolution and present strong biases, a correction is applied for each field. It consists of replacing the mean seasonal cycle of the simulated field by the observed one which has a higher spatial resolution. We proceeded as follows, in a similar way for the PI and $4CO_2$ model fields. We first calculated anomalies of, say, PI solar heat flux Q_{PI}, with respect to the seasonal cycle calculated from the 1960–2000 subperiod of the IPSL-CM4 20C3M simulation (the so-called “climate of the 20th century” control run). This allowed to remove part of the large scale biases present in both the PI and the 20C3M simulations of the IPSL-CM4 model (in particular the inaccurate representation of mean condition in the coastal zone). Last, we added to the anomalies the 1° × 1° COADS climatology for solar heat flux (Da Silva et al. 1994). This procedure is summarized in Eq. 1 for flux Q,

$$Q'_{PI} = Q_{PI} - Q^{clim}_{20C3M} + Q^{clim}_{coads} \qquad (1)$$

It is applied to each variable playing a role in the heat flux formulation: SST, net heat flux, freshwater flux,

Table 1 Large scale oceanic parameters in the Eastern South Pacific from 8 selected coupled OGCMs under the so-called preindustrial climate (PI) and quadrupling CO_2 scenario ($4CO_2$)

OGCM	BCCR		CCMA		CNRM		GFDL		INGV		IPSL		UKMO3		UKMO1	
Scenarios	PI/$4CO_2$		PI/$4CO_2$		PI/$4CO_2$		PI/$4CO_2$		PI/$4CO_2$		PI/$4CO_2$		PI/$4CO_2$		PI/$4CO_2$	
T (years)	250	100	10^3	30	150	30	150	30	100	60	**150**	**40**	150	20	80	80
Z_0 (meters)	30	30	25	25	30	75	25	25	30	30	**35**	**35**	25	25	25	45
dT/dz (10^{-1}°C/m)	2.1	2.3	1.4	1.5	1.0	1.2	2.4	2.6	1.4	1.7	**2.7**	**3.0**	2.0	2.1	2.3	2.8
EUC transport (Sv) at 100°W	17.9	16.9	8.6	8.1	19.4	19.4	16.6	16.4	15.0	16.1	**17.2**	**16.9**	17.6	18.4	24.7	25.7

T the length of the time period (in years) from which the parameters were calculated. Z_0 (in meters) indicates thermocline depth, dT/dz the maximum vertical gradient of temperature (in 10^{-1}°C/m). The OGCMs are BCCR-BCM2.0,CCMA-CGCM3.1(T47), CNRM-CM3,GFDL-CM2.0,INGV-ECHAM4,IPSL-CM4,UKMO-HadCM3,UKMO-HadGEM1

Bold values correspond to IPSL model

surface atmospheric parameters (air temperature, relative humidity) involved in the restoring term dQ/dSST which takes part in the net heat flux formulation (Barnier et al. 1995). It was checked from control experiments that this corrections leads to a more realistic mean SST than when using the direct heat flux outputs because of large errors associated with the misrepresentation of seasonal solar flux by the IPSL-CM4 model near the coast in particular (see Table 2).

Open boundary conditions and initial state values for temperature, salinity, velocity and sea surface height were used to constrain the regional model. Monthly mean outputs of the IPSL-CM4 model were used and linearly interpolated onto the ROMS 1/6° grid using the ROMSTOOLS software (Penven et al. 2008).

The model is run for 33 years for each PI and $4CO_2$ period. The first 3 years of model spin-up are forced by perpetual forcing corresponding to the climatology of the two chosen 10-year periods for the PI and $4CO_2$ scenarios. Then the model is forced by interannual forcing over the two 30-year periods, which are analyzed and compared.

3 Results

3.1 Surface circulation

To illustrate the impact of the dynamical downscaling, the IPSL-CM4 model surface temperature and velocity corresponding to the PI scenario is shown in Fig. 2a and the ROMS solution forced by the IPSL PI solution is shown in Fig. 2b.

Large scale SST biases are noticeable in IPSL-CM4. Coastal upwelling does not occur off Peru and the cold SST pattern off Chile is located ~200–300 km offshore instead of nearshore. The ROMS surface temperature is much more realistic (Fig. 2b). For instance, the regional model is able to represent the cold alongshore SST pattern off Peru. Off Chile, coastal upwelling occurs south of 25°S, in agreement with observed features (Strub et al. 1998). Note that the ROMS temperature averaged over the basin field is 2–3°C cooler than in IPSL-CM4. This is due to the corrected field SST' (see Eq. 1 in Sect. 2) used to restore the model's SST in the heat flux formulation. SST' is cooler than the IPSL-CM4 SST as the COADS SST field is 2–3°C cooler than the IPSL-CM4 20th century climatological SST (not shown). This cooling is also partly due to the enhanced coastal upwelling and offshore advection of cool waters in the ROMS simulations.

The surface circulation is also much more realistic in the ROMS solution. Indeed, an unrealistic poleward surface flow takes place off Peru in the IPSL-CM4 solution (Fig. 2a), whereas the Peru Coastal Current (hereafter PCC) equatorward jet associated with coastal upwelling is present in the ROMS solution (Fig. 2b), in agreement with observed features (Strub et al. 1998). Short scale patterns of 50–100 km such as mesoscale eddies, filaments and jets are also present in ROMS, with a velocity scale comparable to other regional model solutions (e.g. Penven et al. 2005; Colas et al. 2008; Albert et al. 2010).

3.2 Change in vertical structure:

Cross-shore sections near 10°S of ROMS PI and $4CO_2$ mean temperature, salinity and alongshore velocity are presented in Figs. 3 and 4 respectively. These sections illustrate the change in ocean dynamics along the Peruvian coast between 8°S and 13°S. Figure 3 shows that the temperature in the surface layers increased dramatically under anthropogenic forcing. The 16°C isotherm depth in PI is around 70 m 300 km offshore and rises up to 20 m at the coast (Fig. 3a). In $4CO_2$, it is near 200 m depth off shore and deepens towards the coast (Fig. 3b). The nearshore upward tilt of isotherms shows that coastal upwelling takes place in both simulations (Fig. 3). Below ~80 m in PI and $4CO_2$, isotherms tilt downward, denoting the presence of the poleward Peru–Chile Under Current (hereafter PCUC).

The temperature increase is associated with an increase in average vertical thermal stratification in the 0–250 m deep water column, from ~4.5×10^{-2}°C/m in PI to ~5.5×10^{-2}°C/m in $4CO_2$. To further illustrate the changes in thermocline structure, the depth and intensity of the thermocline were estimated offshore of the coastal upwelling from an alongshore-averaged temperature profile. This profile was computed 300 km from the coast and averaged between 8°S and 13°S. The depth of the

Table 2 SST bias and SST root mean square (RMS) for two ROMS simulations performed with a bias correction using an observed climatology (i.e. $Q = Q^{clim}_{coads} + (Q_{2L24} - Q^{clim}_{20C3M})$) and without bias correction (i.e. $Q = Q_{2L24}$)

Area	5°N–20°S (Peru)		20°S–35°S (Chile)	
Heat flux parameterization	No correction	With correction	No correction	With correction
SST bias (in °C)	1.4	−1	−0.7	−1
SST RMS (in °C)	2.3	2	2	2.1

The SST bias and RMS are calculated with respect to the SST Pathfinder climatology (Reynolds and Smith 1994)

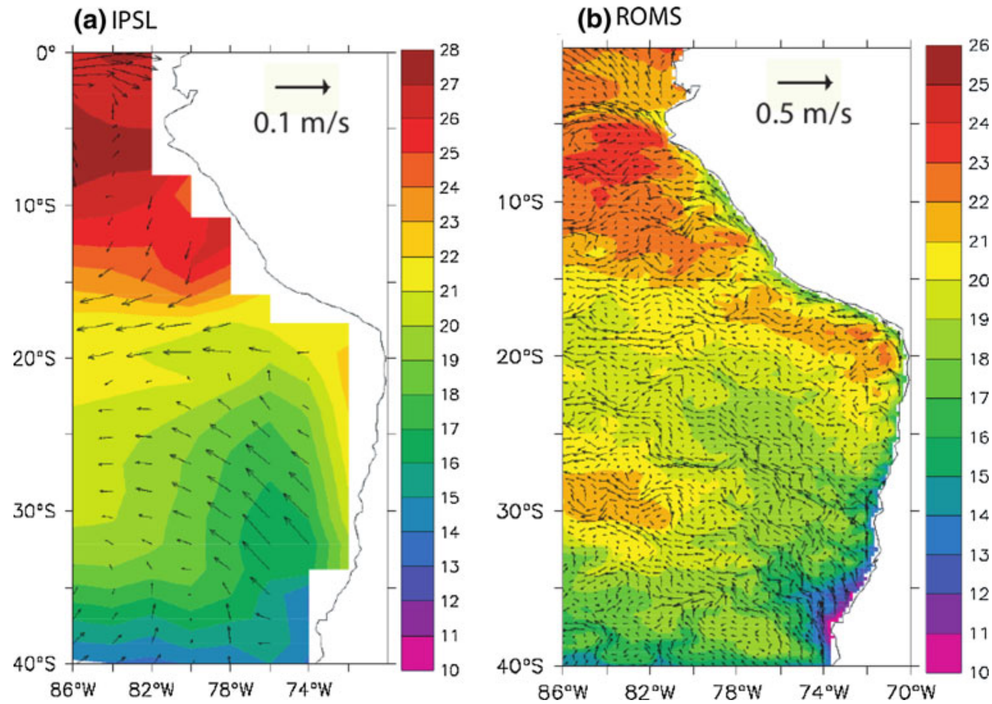

Fig. 2 SST (*color scale* in °C) and horizontal surface velocity (*arrows* in m/s) in **a** IPSL-CM4 PI and **b** ROMS PI in January. Note the change of *color scale* for SST in (**a**) and velocity scale in (**b**)

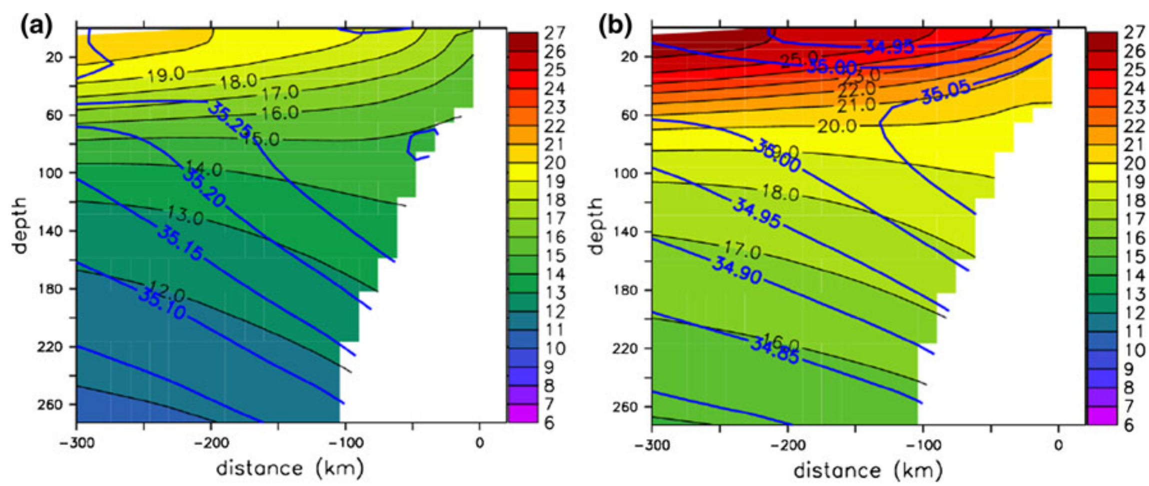

Fig. 3 Mean temperature (*black contours and shading* in °C) and salinity (*blue contours*, in PSU) along a cross-shore section at 10°S for **a** PI and **b** $4CO_2$. Contour interval for temperature (resp. salinity) is 1°C (resp. 0.05 PSU)

thermocline (z_0) is diagnosed as the depth of the maximum vertical temperature gradient (dT/dz for $z = z_0$). Obtained values are listed in Table 3. Thermocline depth remains around 50 m in the PI and $4CO_2$ experiments. In contrast, the intensity of the thermocline (dT/dz for $z = z_0$) increases by 40% in $4CO_2$, from 0.10°C/m in PI to 0.14°C/m in $4CO_2$. We expect this strong stratification increase offshore of the upwelling area to impact the upwelling system by reducing the efficiency of Ekman dynamics.

Strong salinity changes also take place in this area. The PI salinity decreases with depth in the top 250 m, as in Levitus climatological data (not shown), with offshore values around 35.15 psu at 100 m depth and 35.07 psu near 200 m (Fig. 3a). Near the coast, salinity is quite homogeneous and around 35.25 psu, and corresponds to the relatively salty tropical waters advected eastward by the equatorial undercurrent and poleward by the PCUC (not shown). In contrast, fresher waters are present in the whole Eastern South Pacific from 10°N to 30°S in the IPSL-CM4 $4CO_2$ global simulation (not shown). The average depth of the 34.6 psu isohaline over the Eastern South Pacific (15°N–40°S,100°W–70°W) rises from 800 to 1,000 m in the IPSL PI simulation to 200–400 m in the IPSL $4CO_2$ simulation(not shown). Thus, waters with salinities as low

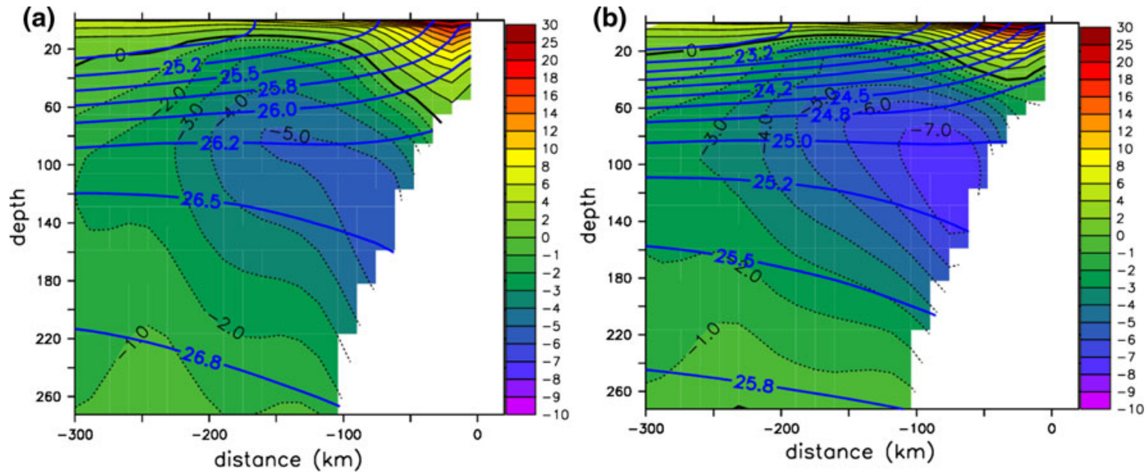

Fig. 4 Density (*blue contours* in kg m^{-3}) and alongshore velocity (*black contours* and *color shading* in cm s^{-1}) on a cross-shore section at 10°S for **a** PI and **b** 4CO_2. Contour interval is 0.25 kg m^{-3} for density, 1 cm s^{-1} for poleward velocity (*dashed*), 2 cm s^{-1} (resp. 5 cm s^{-1}) for equatorward velocity in the [0,20] cm s^{-1} range (resp. [20,30] cm s^{-1} range). Density of pure water (1,000 kg m^{-3}) was substracted from density values

Table 3 Thermocline depth (defined as the depth of maximum vertical gradient of thermocline) and vertical temperature gradient at thermocline depth for an alongshore average, annual mean temperature profile, 300 km from the coast, averaged between 8°S and 13°S off Peru

Simulation name and time period	Thermocline depth (in m)	Temperature gradient intensity (in 10^{-1}°C/m)
PI (1970–1999)	50	1.0
2CO_2 (2070–2079)	50	1.1
4CO_2 (2120–2149)	50	1.4
4CO_2a (2120–2129, PI wind)	50	1.6
4CO_2b (2120-2129, 4CO_2 wind +50%)	50	1.05

as 35.05 psu are upwelled near the shore in the ROMS 4CO_2 simulation (Fig. 3b), whereas they are ~0.20 psu saltier in PI (Fig. 3a). Such modifications of intermediate water characteristics also suggest that strong changes in the nutrient concentration of upwelling source waters may occur.

These hydrological changes are associated with changes in the vertical density structure (Fig. 4). Both temperature and salinity modifications decrease density and increase stratification in the 0–200 m surface layer, the effect of temperature increase being largely dominant. This increase in stratification impacts the alongshore current system. The surface cross-shore density gradient sustains a pressure gradient which forces a thinner PCC in 4CO_2 (~40 m) than in PI (~70 m). The PCUC structure and intensity is also modified. It shoals by ~10–20 m and the undercurrent's core intensifies by ~2 cm s^{-1} in 4CO_2, which represents a ~40% increase.

3.3 Impact on mesoscale circulation

The changes in alongshore currents induces a stronger vertical shear 100–200 km from the coast in the 4CO_2 experiment relative to PI, which impacts baroclinic instability processes (Pedlosky 1987). This is confirmed by the estimation of available potential energy (PE) to eddy kinetic energy (EKE) flux (see Marchesiello et al. 2003 for the detailed mathematical formulation) in the top 100 m in this region (Fig. 5), which is the signature of baroclinic instability. Values are particularly enhanced in fall and winter near the coast, thus showing the important role of the sheared current system (Fig. 4b). Note that mean kinetic energy to EKE flux (characterizing barotropic instability) was also computed but remains almost an order of magnitude smaller than the PE to EKE flux.

In order to illustrate the impact of warming on the mesoscale variability, Fig. 6 displays the mean eddy kinetic energy (hereafter EKE) in the two simulations (see also Table 1 for a quantitative comparison). The map of observed satellite-derived EKE is also presented as a reference. Geostrophic surface velocity anomalies computed from sea level spatial variations are used to derive EKE. EKE for PI displays relatively lower values than the observations, especially off Peru, which is partly related to a lack of intraseasonal variability in the oceanic boundary conditions since monthly average outputs of the IPSL-CM4 model are used. Off Chile, PI EKE amplitude is in relatively good agreement with satellite observations. EKE is underestimated in the 18°S–25°S latitude band and south of 35°S owing to the proximity of the southern open boundary which dampens current instabilities. Notable modifications in EKE patterns are the strong nearshore increase off

Northern Peru (∼30%) and Central Chile (∼38%) in $4CO_2$ with respect to PI (Table 1).

The thickening and intensification of the PCUC, particularly in April-June and August–October (Fig. 7a), plays a major role in this EKE increase by modifying the vertical shear, especially as the equatorward surface PCC mean and seasonal transport varies little (Fig. 7b). The PCUC mean transport increases from 1.9 Sv in the PI experiment to 2.3 Sv in the $4CO_2$ experiment (A ∼20% increase), whereas the EUC transport at 100°W is almost unchanged in the PI (12.7 Sv) and in the $4CO_2$ (12.8 Sv) experiments. In contrast, the seasonal cycle of the PCUC varies in phase with that of the EUC in both the PI and $4CO_2$ experiments (Fig. 7c), likely due to the propagation of equatorial Kelvin waves (Cravatte et al. 2003) and coastal-trapped waves. These results suggest that the eddy kinetic energy change may be explained by changes in two mains dynamical forcings: an increase of the mean PCUC due to the stratification increase in $4CO_2$, and a modification of the equatorially-forced intraseasonal variability in $4CO_2$. The different timing (and possibly intensification) of the coastal waves relatively to the seasonal cycle of the upwelling may impact nearshore EKE (Echevin et al. 2011).

EUC variability, as well as part of the PCUC variability, is controlled by equatorially-forced intraseasonal Kelvin waves propagation which force poleward-propagating coastal trapped waves, and may thus impact nearshore eddy kinetic energy (Echevin et al. 2011).

3.4 Change in upwelling rate

We now investigate how atmospheric momentum and heat forcing modifications translate into upwelling changes. In particular, an increase (decrease) in along-shore winds may not result in a proportional increase (decrease) in upwelling because of potential cross-shore compensating geostrophic adjustment (Marchesiello and Estrade 2010), mixing and restratification processes. Here we test the sensitivity of the vertical flux of mass to the PI and $4CO_2$ atmospheric forcing. The vertical flux of mass is estimated from the maximum vertical velocity between 20 and 50 m depth at the first grid point near the coast (which corresponds to an

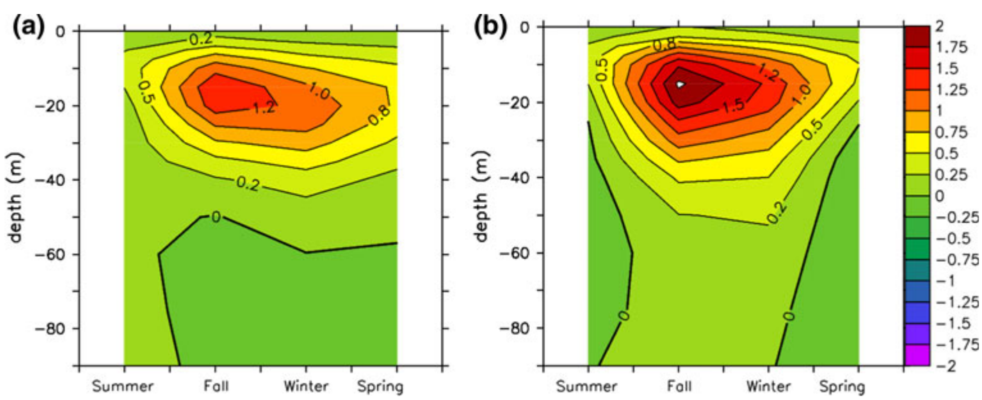

Fig. 5 Time-depth evolution of potential energy (PE) to eddy kinetic energy (EKE) flux (in 10^{-4} cm^2 s^{-3}) for **a** PI and **b** $4CO_2$. PE to EKE flux is calculated for each season and averaged over the domain (84°W–78°W,6°S–10°S] off Northern Peru. Contours every 0.25×10^{-4} cm^2 s^{-3}

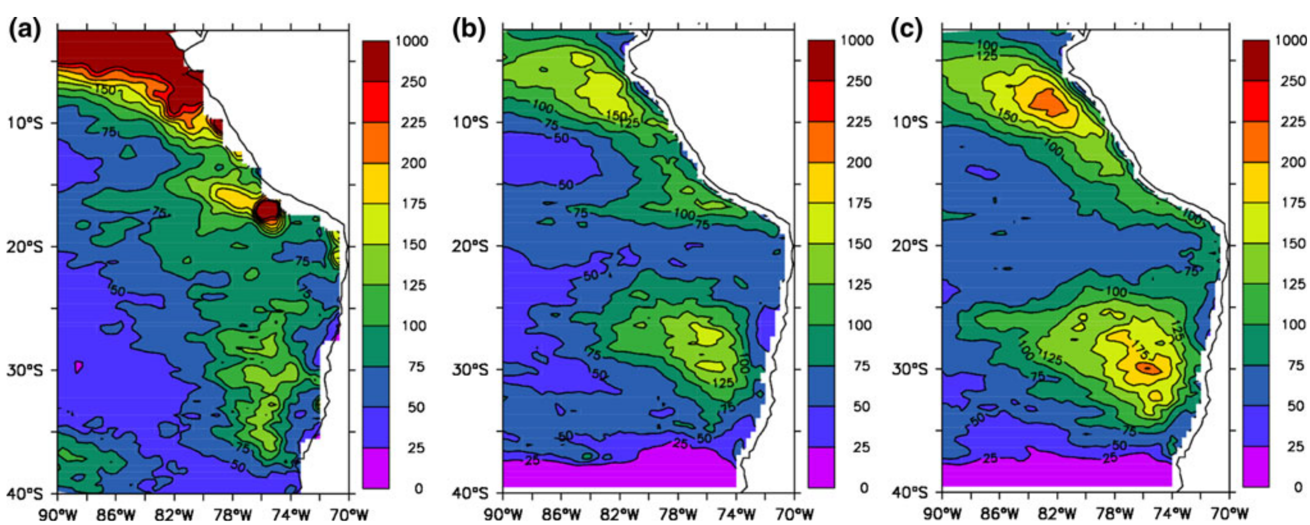

Fig. 6 Mean eddy kinetic energy (EKE, in cm^2 s^{-2}) computed from sea level for **a** AVISO observations over 1992–2004, **b** PI (1970–1999) and **c** $4CO_2$ (2020–2049). Sea level drift has been substracted from $4CO_2$ simulation

18-km wide coastal band). Its seasonal variations are shown in Fig. 8a as a function of latitude. Four main regimes depending on latitude can be identified: the central Peru upwelling regime with maximum upwelling in austral winter between 5°S and 16°S (Chavez 1995), a southern Peru-northern Chile transitional regime with weaker upwelling throughout the year between 16°S and 26°S, and two central Chile regimes with maximum upwelling in austral spring (26°S–32°S), and summer (32°S–37°S) (Strub et al. 1998), driven by the seasonal northward migration of the central Chile Coastal Jet (Garreaud and Muñoz 2005). Note that all these regimes are upwelling-favorable throughout the year, except near 35°S–40°S in late fall-early winter. Qualitatively similar regimes are present in the $4CO_2$ simulation (not shown).

In order to differentiate the changes in upwelling associated with change in wind-stress characteristics and those associated with change in stratification and mixing processes, relative changes in the seasonal variations of Ekman transport and of vertical velocity are presented in Figs. 8b and c. The results indicate that, off central Peru [5°S–18°S], a summer ~10–20% reduction in alongshore upwelling-favorable wind stress (Fig. 8b) from PI to $4CO_2$ leads to a ~20–30% decrease in Ekman vertical velocity (Fig. 8c). The more intense winter upwelling increases moderately (~10%) in $4CO_2$, proportionally to the ~5–10% wind stress increase. Off northern Chile [20°S–28°S], the weak upwelling rate (less than 2 m day^{-1}, Fig. 8a) responds quasi-linearly to the wind stress increase, except at some specific latitudes where the local increase is higher (e.g. the ~50–100% increase near 25°S, Fig. 8c). Further south [26°S–40°S], the intense summer upwelling shows a strong increase of up to 20–30% in $4CO_2$, proportional to the increase in wind stress forcing.

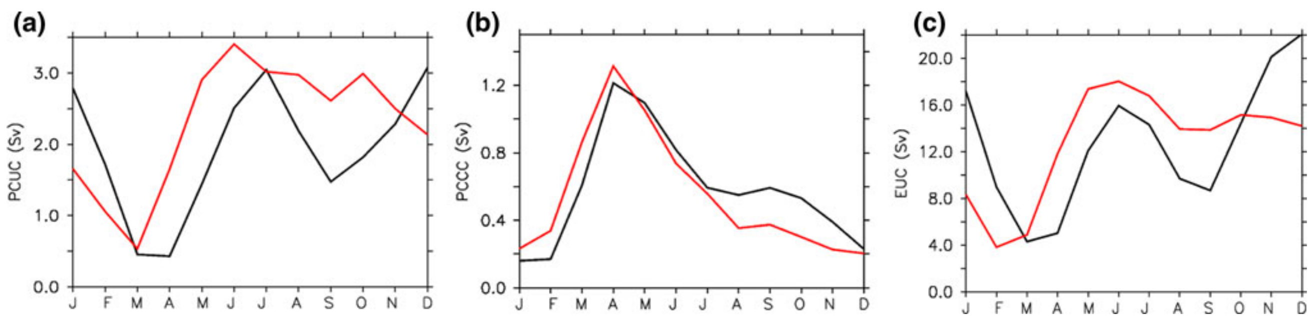

Fig. 7 Transport seasonal variations (in Sv) for **a** PCUC, **b** PCC and **c** EUC at 100° for PI (*black line*) and $4CO_2$ (*red line*). PCUC (PCC) transport was computed by summing poleward (equatorward) flow through an averaged cross-shore section between 6°S and 12°S, and 0–350 m (0–200 m) depth. EUC transport was computed by summing eastward flow through through a 4°N–4°S meridional section at 100°W, between 0 and 200 m depth

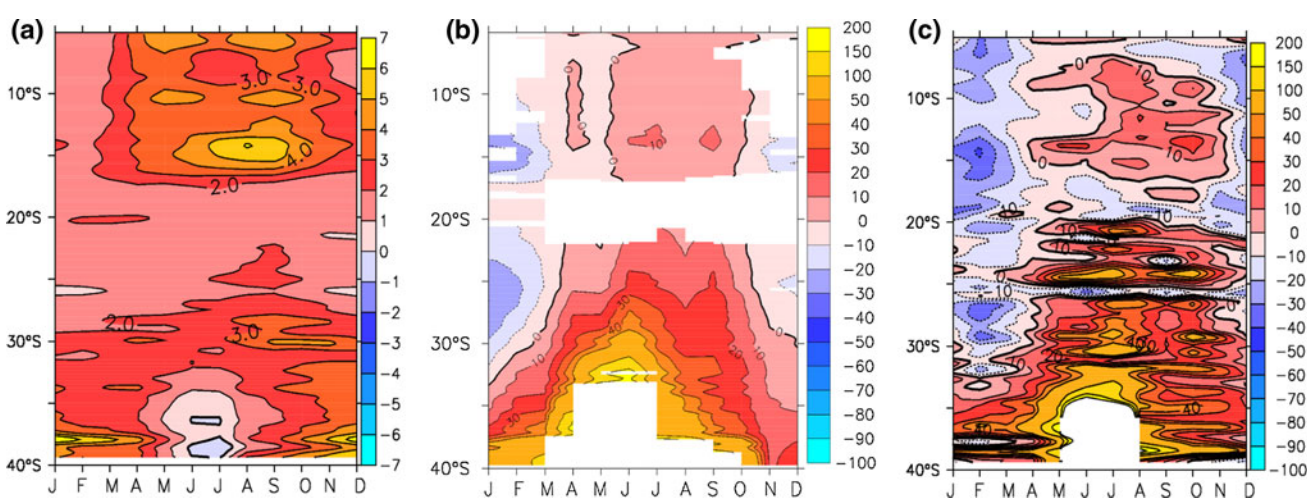

Fig. 8 Time-latitude variations of **a** PI coastal upwelling (in m day^{-1}), relative change (in %) between $4CO_2$ and PI in **b** Ekman transport, and in **c** coastal upwelling, relative to PI. Coastal upwelling is derived from maximum model vertical velocity at the coast between 20 and 50 m depth, and Ekman transport from alongshore wind stress. Model vertical velocities have been smoothed alongshore with a running mean over 11 grid points to filter noisy patterns. Values have been masked when the PI alongshore wind stress (resp. vertical velocity) is less than 5×10^{-2} N m^{-2} (resp. 5 cm day^{-1})

3.5 Sensitivity experiments using $2CO_2$ scenario and modified alongshore wind stress off Peru

One may argue that the climate scenario investigated here is rather extreme and that conclusions may be different under less drastic warming conditions. To investigate this aspect, an ad hoc numerical experiment was conducted using ocean conditions and downscaled wind stress from the IPSL-CM4 $2CO_2$ scenario. In this simulation, $2CO_2$ wind increase is more moderate off Chile and almost unchanged off Peru compared to that in $4CO_2$ (see Fig. 8a in Goubanova et al. (2010)). However, due to changes in large scale and local thermal stratification, the thermocline intensity increases slightly (10%, Table 3), and the EKE increase with respect to PI is important (+17%, +5%, +35% for Northern Peru, Northern Chile, Central Chile, respectively, see Table 4).

The moderate summer upwelling decrease off Peru in our ROMS simulations (Fig. 8c) illustrates the sensitivity of the dynamical response to the 10% decrease in upwelling-favorable wind forcing as diagnosed by Goubanova et al. (2010). The latter study contrasts with Bakun's (1990) hypothesis suggesting greenhouse-associated intensification of thermal low-pressure cells over the coastal landmasses and therefore increase in upwelling favourable winds in a warmer climate (Bakun et al. 2010). In order to investigate the sensitivity of the upwelling dynamics to a potential increase in wind stress forcing, two simulations (referred to as $4CO_2$a and $4CO_2$b) were performed using a modified wind stress. In $4CO_2$a, the wind stress is replaced by the PI seasonal wind stress field, therefore assuming no change in alongshore wind stress under $4CO_2$ warmer conditions. In $4CO_2$b, the $4CO_2$ wind stress is increased by 50% in a 1,000 km-width band along the Peru–Chile coast. It varies smoothly to reach standard $4CO_2$ values 1,000 km away from the coast. In this experiment, the stronger alongshore wind stress (with respect to the standard $4CO_2$ experiment) is expected to upwell deeper colder waters and to enhance vertical mixing, which could limit surface stratification, modify both the current system and the mesoscale circulation. Note that in the $4CO_2$a and $4CO_2$b sensitivity experiments, net heat fluxes (including the SST used for restoring) were kept identical to those of the standard $4CO_2$ experiment.

Thermocline intensity increases by $\sim$14% in $4CO_2$a with respect to $4CO_2$ (Table 3), likely because of the slightly (10%) weaker winter wind stress off Peru in $4CO_2$a than in $4CO_2$ (Fig. 8b). In experiment $4CO_2$b, thermocline intensity ($\sim 1.05 \times 10^{-1}$°C/m) matches that of the PI simulation ($\sim 1.0 \times 10^{-1}$°C/m). It is much lower than that of the $4CO_2$ simulation ($\sim 1.4 \times 10^{-1}$°C/m), which is likely due to the intensified wind-induced vertical mixing in $4CO_2$b. Thus, in the case of a strong (+50%) wind stress increase, vertical mixing may compensate the impact of greenhouse-induced surface heating on thermocline intensity. Note that the depth of the thermocline ($\sim$50 m) is not modified in these experiments (Table 3).

Alongshore-averaged (between 6°S and 13°S) density and alongshore velocity changes are compared in Fig. 9. Density structure changes little in $4CO_2$a (less than -0.05 kg m^{-3}) over the top 100 m (Fig. 9a) in comparison to the standard $4CO_2$ experiment. In $4CO_2$b, density difference reaches +0.1 kg m^{-3} at $\sim$40–80 m depth, indicating upwelling of denser water on the shelf than in $4CO_2$, and $\sim$0.3 kg m^{-3} near the surface, indicating mixing and surface cooling. The surface coastal current decreases by $\sim$2 cm/s in $4CO_2$a (Fig. 9b), and increases by up to 8 cm/s in $4CO_2$b. The PCUC is also modified (Fig. 9c): its core velocity near 60 m (resp. $\sim$120–140 m) reaches $\sim$8 cm/s (resp. $\sim$9 cm/s) in $4CO_2$a (resp. $4CO_2$b) instead of $\sim$6–7 cm/s at $\sim$120 m in $4CO_2$. All three $4CO_2$ simulations generate an EKE increase with respect to PI off Northern Peru ($\sim$+19% and $\sim$+63% for $4CO_2$a and $4CO_2$b, respectively, see Table 4) as in the $4CO_2$ experiment ($\sim$+30%).

Figure 10 illustrates the sensitivity of vertical velocity off the Peruvian shelf [6°S–14°S] to the different alongshore wind stresses. The $4CO_2$a upward flux is increased with respect to $4CO_2$ during summer and fall, and remains very similar to the PI flux until July. It then decreases between July and December and becomes comparable with that in the $4CO_2$ experiment in spite of the stronger wind forcing in $4CO_2$a than in $4CO_2$. This suggests that the large scale ocean conditions or the wind forcing could play a dominant role depending on the season in the $4CO_2$ scenario. In contrast, when the wind stress is strongly enhanced (by 50% in $4CO_2$b with respect to $4CO_2$), the wind-driven upwelling clearly dominates and the vertical flux increases linearly by $\sim$ 50%.

4 Discussion and conclusions

The regional ocean circulation in the HCS was studied using a regional circulation model forced by two idealized climate scenarios, the preindustrial and the CO_2 quadrupling scenario from the IPSL-CM4 global climate model. The most striking results of these experiments are (1) a strong heating of more than 4°C in the upper ocean off Peru, from the surface to 300 m depth, (2) an increase in surface density stratification and thermocline intensity, inducing (3) a thinner surface Peru Coastal Current, (4) an intensified poleward undercurrent, (5) an enhanced mesoscale turbulence driven by the enhanced vertical shear of the coastal current system, (6) a summer decrease and moderate winter increase in coastal upwelling off Peru, and

Table 4 EKE average values (in $cm^2\ s^{-2}$) in 3 nearshore areas: North Peru (85°W–76°W; 6°S–12°S); South Peru (80°W–72°W; 12°S–18°S); Central Chile (80°W–70°W; 25°S–35°S)

Simulation name and time period	EKE (Northern Peru)	EKE (Southern Peru)	EKE (Central Chile)
PI (1970–1999)	114.2	97.3	97.8
PI (1970–1979)	92.5	90.9	84.4
PI (1980–1989)	122.3	96.0	91.0
PI (1990–1999)	108.5	88.0	97.4
$4CO_2$ (2120–2149)	148.9 (+30%)	100.2 (+3%)	135.5 (+38%)
$4CO_2$ (2120–2129)	141.1	98.8	120.0
$4CO_2$ (2130–2139)	145.9	93.6	104.7
$4CO_2$ (2140–2149)	139.5	91.6	155.1
$2CO_2$ (2070–2079)	133.3 (+17%)	102.0 (+5%)	132.4 (+35%)
$2CO_2$ (2050–2059)	125.4	88.2	125.5
$2CO_2$ (2060–2069)	125.0	101.7	130.1
$2CO_2$ (2070–2079)	131.3	100.3	113.3
$4CO_2$a (2120–2129, PI wind)	135.8 (+19%)	108.6 (+12%)	117.9 (+20%)
$4CO_2$b (2120–2129, $4CO_2$ wind +50%)	185.7 (+63%)	126.8 (+30%)	197.0 (+101%)

EKE was also calculated for 3 distinct decades to illustrate interdecadal variability and demonstrate the robustness of the EKE increase with warming. Percentage are calculated with respect to the PI 1970–1999 values

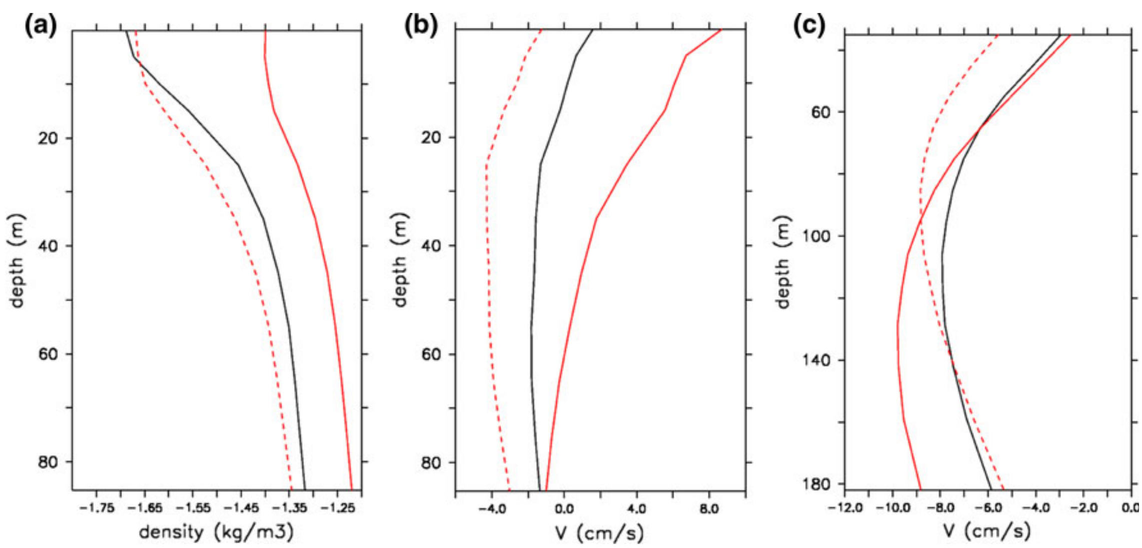

Fig. 9 Mean alongshore-averaged **a** density (in kg m^{-3}) and **b** alongshore velocity (in cm s^{-1}, positive is equatorward) anomalies with respect to PI, in the equatorward current, 40 km from the coast. **c** Mean alongshore-averaged total alongshore velocity (in cm s^{-1}, negative is poleward) in the coastal undercurrent's core, 80 km from the coast, for $4CO_2$ (*full black line*), $4CO_2$a (*dashed red line*), $4CO_2$b (*full red line*). Alongshore averaged is performed between 6°S and 12°S

(7) a strong spring-summer increase in upwelling off Central Chile.

Sensitivity experiments on the wind stress forcing suggest that, in the conditions of the $4CO_2$ IPSL-CM4 warming scenario, an increase of up to 50% in upwelling-favorable wind stress does compensate for thermocline intensity because of the enhanced mixing, but does not compensate for the impact of the surface warming on the intensity of the mesoscale circulation. It also shows that the coastal upwelling response to moderate wind stress variations from contrasted wind scenarios is nonlinear and may depend on the season.

Note that surface cooling by increased latent heat flux was not taken into account in these sensitivity experiments. Net heat flux into the ocean, which includes implicitly cooling due to the latent heat flux, is prescribed by $4CO_2$ conditions. Taking into account the extra latent heat cooling related to the increase in wind stress in $4CO_2$a and $4CO_2$b could somewhat decrease surface stratification. Further investigation of this process requires taking into

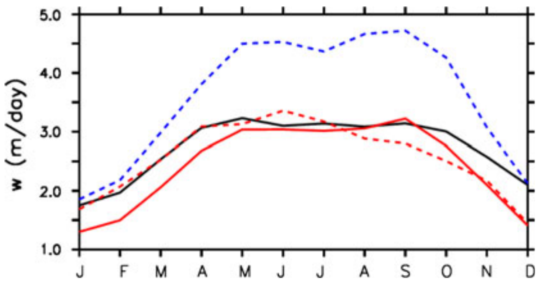

Fig. 10 Seasonal variations of vertical velocity (in m/day) for the Peru region, averaged between 6°S and 14°S, for PI (*black line*), $4CO_2$ (*red line*), $4CO_2$a (*red dashed line* $4CO_2$ oceanic conditions with PI wind stress) and $4CO_2$b (*blue dashed line* $4CO_2$ oceanic conditions with $4CO_2$ wind stress increase by 50% in coastal band, see text)

account the feedbacks associated with latent heat flux and explicitly model it using bulk formulas. This will be done in future work.

The depth of the thermocline, diagnosed in our simulations by the depth of the maximum vertical thermal gradient 300 km offshore of the Peru shore, is remarkably stable (~50 m) in all simulations, even in the case of a strong wind increase (experiment $4CO_2$b). This suggests that the nutricline depth, which should range with the thermocline depth, might change relatively little under climate warming. Consequently, a parameter more crucial for biological productivity than change in thermocline depth could be the change in nutrient content for the water masses upwelled at the coast. These waters, transported by the Peru undercurrent (Albert et al. 2010) were shown to originate from the equatorial area (Montes et al. 2010). However, investigating the modification of subsurface water mass characteristics in the Equatorial Pacific induced by global warming is another field of research clearly beyond the scope of the present work. However, it is worthy to note that the model vertical discretization is restricted by the number of sigma levels (31 on our case). This limitation might somewhat hamper an accurate representation of the thermocline position. Sensitivity tests to this parameterization will be done in a future study.

This study, as that of Goubanova et al. (2010) also confirms that the Peru and Chile upwelling systems behave differently with regards to their sensitivity to climate change. The increase in upwelling rates off Chile (25°S–40°S; Fig. 8b) is related to an intensification of the alongshore surface pressure gradient due to an increase in atmospheric surface pressure south of the SEP anticyclone (Garreaud and Falvey 2009). Off Peru the dynamical processes are less clear. Part of the summer upwelling-favorable wind decrease might be related to the decrease in Walker circulation (Vecchi and Soden 2007; Vecchi et al. 2006). This decrease is partly compensated by the winter equatorward migration of the SEP anticyclone, which has a greater influence on Peru coastal winds during this season.

The simulated changes in upwelling rate obtained in this study, whereas they are consistent with observations of the past 50 years for the Chilean region (Falvey and Garreaud 2009), contrast with results from a recent study based on in situ measurements of SST, wind reanalyses, and Alkenone-based SST reconstruction off Pisco (14°S) (Gutierrez et al. 2011). The authors show a 50-year trend of decreasing SST, which suggests a long-term upwelling-favorable trend despite the strong interannual and interdecadal variability in the wind forcing. Nevertheless, it is difficult to compare this study with ours since our work does not focus on modern time periods and is based on idealized climate scenarios which do not represent the observed decadal variability. A promising approach would be to perform regional simulations forced by NCEP/NCAR (Kalnay et al. 1996) and ERA40 (Uppala et al. 2005) reanalysis over the last 50 years. This work is under way.

Despite the differences in experimental set up, it is interesting to compare our results with similar experiments performed for the California EBUS. Auad et al. (2006) found that mixing due to an anthropogenically-forced increase in upwelling-favorable winds overcomes stratification caused by surface heating. This led to a greater upwelling rate and a decrease in EKE. This contrasts with the results presented here, even for the Chilean region where upwelling increases in warmer conditions. This might be due to the moderate heating taking place in their case, which consisted in a 36% CO_2 increase from present day concentrations, versus 200–400% CO_2 increase from preindustrial concentrations in our case. On the other hand, it must be noted that Di Lorenzo et al. (2005)'s study found an EKE increase over 1949–2000 using a similar model configuration than Auad et al. (2006). Decadal variability in EKE could partially hinder the anthropogenically-forced climate signals, and more model studies contrasting hindcasts simulations and downscaling of climate scenarios are needed to confirm these tendencies.

Despite limitations owed to model biases and experimental set-up (in particular the fact that regional air-sea feedback are not taken into account), the model experiments performed in this work offer the opportunity to document the sensitivity of the ecosystem to change in simulated environment conditions. Underway coupling of our dynamical model with biogeochemical (Echevin et al. 2008) and biological models (Brochier et al. 2008; Hernandez et al. 2010) will allow to further investigate the impact of regional climate change on the planktonic biomass, the oxygen minimum zone, and higher trophic levels.

Acknowledgments Numerical simulations were performed on the IDRIS NEC-SX8 calculator. V. Echevin and B. Dewitte are funded by the Institut de Recherche pour le Développement (IRD). K. Goubanova was supported by the AXA foundation. A. Belmadani was cofunded by the IRD Département de Soutien et Formation (DSF), Collecte Localisation Satellites (CLS). All authors received support from the PCCC and PEPS-VMCS2008 ANR projects during the development of this work. F. Colas is acknowledged for providing the matlab routines used to calculate the barotropic and baroclinic instability energy conversion terms.

References

Albert A, Echevin V, Lévy M, Aumont O (2010) Impact of nearshore wind stress curl on coastal circulation and primary production in the Peru upwelling system. J Geophys Res 115:C12033. doi: 10.1029/2010JC006569

Auad G, Miller A, Di Lorenzo E (2006) Long-term forecast of oceanic conditions off California and their biological implications. J Geophys Res 111:C09008. doi:10.1029/2005JC003219

Bakun A (1990) Global climate change and intensification of coastal ocean upwelling. Science 247:198–201

Bakun A (1996) Patterns in the ocean. Ocean processes and marine population dynamics. University of California Sea Grant, California, USA, in cooperation with Centro de Investigaciones Biologicas de Noroeste, La Paz, Baja California Sur, Mexico, 323 pp

Bakun A, Weeks S (2008) The marine ecosystem off Peru: What are the secrets of its fishery productivity and what might its future hold? Prog Oceanogr 79:290–299

Bakun A, Field D, Renondo-Rodriguez A, Weeks S (2010) Greenhouse gas, upwelling favourable winds, and the future of upwelling systems. Global Change Biol 16(4):1213–1228

Barnier B, Siefridt L, Marchesiello P (1995) Thermal forcing for a global ocean circulation model using a three-year climatology of ECMWF analyses. J Mar Syst 6:363–380

Belmadani A, Dewitte B, An SI (2010) ENSO feedbacks and associated timescales of variability in a multi-model ensemble. J Clim 23(12):3181–3204

Brochier T, Lett C, Tam J, Fréon P, Colas F, Ayon P (2008) An individual-based model study of anchovy early life history in the northern Humboldt current system. In: Werner F, Lough RG, Bertrand A, Guevara Carrasco R, Soler P, Csirke J, Chavez FP (eds) The northern Humboldt current system: ocean dynamics, ecosystem processes and fisheries. Prog Oceanogr 79:313–325

Carr M-E, Kearns E (2003) Production regimes in four eastern boundary current systems. Deep Sea Res II 50(22–26): 3199–3221

Chavez FP (1995) A comparison of ship and satellite chlorophyll from California and Peru. J Geophys Res 100(C12):24855–24862

Chavez FP, Messié M (2009) A comparison of eastern boundary upwelling ecosystems. Prog Oceanogr 83:80–96

Chavez FP, Ryan J, Lluch-Cota SE, Niquen M (2003) From anchovies to sardines and back: multidecadal change in the Pacific Ocean. Nature 299:217–221

Chavez FP, Bertrand A, Guevara-Carrasco R, Soler P, Csirke J (2008) The northern Humboldt Current system: brief history, present status and a view towards the future. Prog Oceanogr 79:95–105

Colas F, Capet X, McWilliams JC, Shchepetkin AF (2008) 1997–1998 El Niño off Peru: a numerical study. Prog Oceanogr 79:138–155

Cravatte S, Picaud J, Eldin G (2003) Second and first baroclinic Kelvin modes in the equatorial pacific at intraseasonal times scales. J Geophys Res 108(C8):3266. doi:10.1029/2002JC001511

Da Silva AM, Young CC, Levitus L (1994) Atlas of surface marine data 1994, vol 1, Algorithms and procedures, technical report. National Oceanic and Atmospheric Administration, Silver

Di Lorenzo E, Miller AJ, Schneider N, McWilliams JC (2005) The warming of the California current: dynamics, thermodynamics and ecosystem implications. J Phys Oceanogr 35:336–362

Echevin V, Aumont O, Ledesma J, Flores G (2008) The seasonal cycle of surface chlorophyll in the Peruvian upwelling system: A modelling study. Prog Oceanogr 79:167–176

Echevin V, Colas F, Chaigneau A, Penven P (2011) Sensitivity of the Northern Humboldt Current system nearshore modelled circulation to initial and boundary conditions. J Geophys Res (in review)

Falvey M, Garreaud R (2009) Regional cooling in a warming world: Recent temperature trends in the southeast Pacific and along the west coast of subtropical South America (1979–2006). J Geophys Res 114:D04102. doi:10.1029/2008JD010519

Garreaud R, Falvey M (2009) The coastal winds off western subtropical South America in future climate scenarios. Int J Climatol 29:543–554. doi:10.1002/joc.1716

Garreaud R, Muñoz R (2005) The low-level jet off the subtropical west coast of South America: Structure and variability. Mon Wea Rev 133:2246–2261

Gordon C, Cooper C, Senior CA, Banks HT, Gregory JM, Johns TC, Mitchell JFB, Wood RA (2000) The simulation of SST, sea ice extents and ocean heat transports in a version of the Hadley Centre coupled model without flux adjustments. Clim Dyn 16:147–168

Goubanova K, Echevin V, Dewitte B, Codron F, Takahashi K, Terray P, Vrac M (2010) Statistical downscaling of sea-surface wind over the Peru-Chile upwelling region: diagnosing the impact of climate change from the IPSL-CM4 model. Clim Dyn. doi: 10.1007/s00382-010-0824-0

Guilyardi E (2006) El Nino-mean state-seasonal cycle interactions in a multi-model ensemble. Clim Dyn 26:329–348

Guilyardi E, Wittenberg A, Fedorov A, Collins M, Wang C, Capotondi A, van Oldenborgh GJ, Stockdale T (2009) Understanding El Niño in ocean-atmosphere general circulation models: progress and challenges. Bull Am Meteor Soc 90(3):325–340

Gutierrez D, Bouloubassi I, Sifeddine A, Purca S, Goubanova S, Graco M, Field D, Méjanelle L, Velazco F, Lorre A, Salvatteci R, Quispe D, Vargas G, Dewitte B, Ortlieb L (2011) Coastal cooling and increased productivity in the main upwelling zone off Peru since the mid-twentieth century, Geophys Res Lett (in press)

Hernandez O, Lehodey P, Senina I, Bertrand A, Castillo R, Echevin V, Gaspar P (2010) Modelling anchovy population in the Humboldt upwelling system, PICES conference, climate change effects on fish and fisheries: forecasting impacts, assessing ecosystem responses, and evaluating management strategies, April 25–29, Sandai, Japan

Hourdin F, Musat I, Bony S, Braconnot P, Codron F, Dufresne JL, Fairhead L, Filiberti MA, Friedlingstein P, Grandpeix JY, Krinner G, LeVan P, Li ZX, Lott F (2006) The LMDZ4 general circulation model: climate performance and sensitivity to parametrized physics with emphasis on tropical convection. Clim Dyn 27(7–8):787–813

Jones RG, Noguer M, Hassell DC, Hudson D, Wilson SS, Jenkins GJ, Mitchell JFB (2004) Generating high resolution climate change scenarios using PRECIS. Met. Office Hadley Centre, Exeter, p 40

Kalnay E, Kanamitsu M, Kistler R et al (1996) The NCEP/NCAR 40-year reanalysis project. Bull Am Meteor Soc 77:437–471

Madec G, Delecluse P, Imbard M, Lévy C (1998) OPA 8.1 ocean general circulation model reference manual. Notes du pôle de modélisation, laboratoire d'océanographie dynamique et de climatologie, Institut Pierre Simon Laplace des sciences de l'environnement global, 11 Dec 1998

Marchesiello P, Estrade P (2010) Upwelling limitation by coastal divergence. J Mar Res (in press)

Marchesiello P, McWilliams JC, Shchepetkin A (2003) Equilibrium structure and dynamics of the California Current System. J Phys Oceanogr 33:753–783

Marti O, Coauthors (2010) Key features of the IPSL ocean atmosphere model and its sensitivity to atmospheric resolution. Clim Dyn 34:1–26

Meehl GA, Covey C, Delworth T, Latif M, McAvaney B, Mitchell JFB, Stouffer RJ, Taylor KE (2007a) The WCRP CMIP3 multimodel dataset: a new era in climate change research. Bull Am Meteor Soc 88(9):1383–1394

Meehl GA, Covey C, Delworth T, Latif M, McAvaney B, Mitchell JFB, Stouffer RJ, Taylor KE (2007b) Global climate projections. In: Solomon SD et al (eds) Climate change 2007: The physical science basis. Cambridge University Press, Cambridge, pp 747–845

Montes I, Colas F, Capet X, Schneider W (2010) On the pathways of the equatorial subsurface currents in the eastern equatorial Pacific and their contribution to the Peru–Chile undercurrent. J Geophys Res 115:C09003. doi:10.1029/2009JC005710

Nakicenovic N, Coauthors (2000) Special report on emissions scenarios: A special report of working group III of the intergovernmental panel on climate change. Cambridge University Press, Cambridge, p 599

Pedlosky J (1987) Geophysical fluid dynamics, 2nd edn. Springer, Berlin 710 p

Penven P, Echevin V, Pasapera J, Colas F, Tam J (2005) Average circulation, seasonal cycle, and mesoscale dynamics of the Peru Current System: A modeling approach. J Geophys Res 110(C10): C1002110. doi:1029/2005JC002945

Penven P, Marchesiello P, Debreu L, Lefevre J (2008) Software tools for pre- and post-processing of oceanic regional simulations. Environ Model Softw 23:660–662

Pope V, Gallani ML, Rowntree PR, Stratton RA (2000) The impact of new physical parameterizations in the Hadley centre climate model: HadAM3. Clim Dyn 16:123–146

Reynolds RW, Smith TM (1994) Improved global sea surface temperature analyses using optimum interpolation. J Clim 7:929–948

Shchepetkin AF, McWilliams JC (2005) The regional oceanic modeling system: A split-explicit, free-surface, topography-following-coordinate ocean model. Ocean Model 9:347–404

Smith WHF, Sandwell DT (1997) Global seafloor topography from satellite altimetry and ship depth soundings. Science 277:1957–1962

Snyder MA, Sloan LC, Diffenbaugh NS, Bell JL (2003) Future climate change and upwelling in the California Current. Geophys Res Lett 30(15):1823. doi:10.1029/2003GL017647

Strub PT, Mesias JM, Montecino V, Rutllant J, Salinas S (1998) Coastal ocean circulation off western South America. In: Robinson AR, Brink KH (eds) The Sea, vol 11. Wiley, New York, pp 273–314

Uppala S, KAllberg PW, Simmons AJ et al (2005) The ERA-40 reanalysis. Quart J R Meteor Soc 131:2961–3012

van Oldenborgh GJ, Philip SY, Collins M (2005) El Niño in a changing climate: a multi-model study. Ocean Sci 1:81–95

Vecchi GA, Soden BJ (2007) Global warming and the weakening of tropical circulation. J Clim 20:4316–4340

Vecchi GA, Soden BJ, Wittenberg AT, Held IM, Leetmaa A, Harrison MJ (2006) Weakening of tropical Pacific atmospheric circulation due to anthropogenic forcing. Nature 441:73–76. doi:10.1038/nature04744